

Finite-element view-factor computations for radiant energy exchanges

T. Muneer^{1b)}, S. Ivanova^{2 b)}, Y. Kotak^{3 a)} and M. Gul^{3 b)}

¹*Edinburgh Napier University, 10 Colinton Road, EH10 5DT, Edinburgh, United Kingdom*

²*University of Architecture, Civil Engineering and Geodesy, Sofia, Bulgaria*

³*Heriot-Watt University, EH14 4AS, Edinburgh, United Kingdom*

ABSTRACT

Radiation heat transfer has very many applications within the building services sector. CIBSE Guide A provides the physics background and the relevant mathematical functions for radiant energy exchanges between surfaces of different configurations in chapters 2 and 5. The aim of this article is to present procedures for inter-surface radiant energy exchange that range from the most simple (macro-) to most general formulations that are based on a micromesh, finite-element approach. The justification for such detailed procedures and their applicability within the modern building energy simulation software is also covered.

Keywords: view factor, reflected radiation, finite elements, building energy simulation, radiant energy exchange

I. INTRODUCTION

In any given society buildings in general have been identified to be one of the most energy consuming sector. Within the EU28 it has been reported¹ that buildings are responsible for over 50% of the gross energy budget. Furthermore, the bulk of the above proportion of energy use may be attributed to heating or cooling of buildings.

There has been a demand by the respective national governments to address the above issue of such large-scale energy consumption and numerous legislation related instruments were introduced to encourage energy efficiency. The building services community has responded to the above challenge and one of the positive actions undertaken was refining of building energy simulation tools. As a result, over the past few -

a) Author to whom correspondence should be addressed. Electronic mail: yk78@hw.ac.uk

b) T. Muneer, S. Ivanova and M. Gul contributed equally to this work.

decades the software tools have evolved from being part-physics, part-empirical to tools that use the physical laws in a more fundamental manner. Examples that may be cited here are Computational Fluid Dynamics (CFD) tools for solving air-flow problems and daylighting software such as RADIANCE.

CFD simulation software allows to predict the impact of fluid flow on any product throughout the design and manufacturing as well as during end use. It works on the phenomena like studying single or multi-phase, isothermal or reacting, compressible or not by giving valuable insight into product performance.

RADIANCE software is used for the analysis and visualization of lighting design. The primary advantage of this software is there are no limitations on the geometry or to materials that may be simulated. It is used by architects and engineers to predict illumination, visual quality and appearance of innovative design space and by researchers to evaluate new lighting and daylight technologies.

In a recent publication the present research team has presented a case for obtaining building cooling load profile from a numerical solution of the fundamental heat conduction equation². Another example that may be cited here is the work of Laccarino et al (2010)³ who developed a building energy model that coupled a CFD tool with heat transfer information from an energy simulation tool. Their intention was to produce an integrated CFD- energy simulation model. Their model was then validated using data from monitored buildings in California. The above report is also available at Stanford University⁴.

The above-mentioned, recursive and computer-intensive developments have only been possible due to the exponential rise of computing power and its cost reduction. A brief review of the latter would therefore be not out of order at this stage.

The highest performing computing machines that are currently in use hundreds of thousands of processing cores and are capable of 10^{15} (petaflop) floating point operations per second. That is a thousand times more than the most powerful machine of 2000, which in turn were a thousand times more than a decade before that.

Researchers associated with the US Government Sandia Advance Devices Technologies laboratory⁵ have assessed that today's (2014) desktop computing cost of 181MFlops/\$ will drop to 18GFlops/\$ by the year 2030. The average current microprocessor clock speeds would also increase to 33GHz by the year 2015. For supercomputers the main demand for increasing computing speed is from the climate change modelling community. However, the building energy simulation would benefit from such developments. The Edinburgh-based supercomputing facility⁶ is forecasting an increase of computing power from today's Petflops to Exaflops

by year 2020 while Sandia's researchers are predicting a performance of the order of Zettaflops (10^{21}) for the year 2030.

However, there are certain challenges that lie ahead. It is being predicted that the high performance exascale computing machines will have different architectures from that which has dominated for the last decade and more. There will be an impact on software; existing software will most likely need to be rewritten⁷. Therefore, in brief, due to increased computing power that is now available at ever decreasing cost there is a general trend towards the incorporation of fundamental physical laws and processes, rather than use of empiricism within building energy simulation tools. Within the CIBSE Guides design charts related to radiation exchange between surfaces that are either parallel or perpendicular to each other are presented. Those charts are somewhat restrictive though and do not allow for estimation of energy exchange for surfaces facing each other at an acute or obtuse angle. Furthermore, the issue of ground-reflected radiation that is incident upon tilted solar thermal and photovoltaic collectors has not been addressed within existing literature appropriately. On occasions, there are also incidences where radiation reflected off any given building's glass façade is of interest. An interesting example that may be cited herein is that of a new London skyscraper that has been blamed for reflecting light which melted parts of a car parked on a nearby street⁸. One of the present research team members was asked to provide preliminary advice regarding analysis of that problem.

To summarise therefore there are at least two areas of applicability of radiation energy exchange for the proposed work:

- (i) sol-air temperature and building cooling load due to energy exchange from ground and neighbouring building surfaces;
- (ii) energy balance of solar thermal collectors and PV modules, once again taking into account the ground-reflected solar radiation.

The aim of this article is to present procedures for inter-surface radiant energy exchange that range from the most simple (macro-) to most general formulations that are based on a micromesh, finite-element approach.

II. ANALYSIS

A. Radiation exchange between any two surfaces

For any two black surfaces the thermal radiation exchange is given by Eq. (1):

$$Q_{1-2} = \sigma(T_1^4 - T_2^4)A_1F_{1-2} = \sigma(T_2^4 - T_1^4)A_2F_{2-1} \quad (1)$$

Within Heat Transfer terminology the term F_{1-2} is known as "configuration factor" (CF)⁹. There are also other names for the latter such as "view factor", "geometry factor", "angle factor" or "shape factor". For any two elemental surfaces such as those shown in Fig. 1, F_{1-2} is given as Eq. (2):

$$F_{1-2} = \frac{1}{A_1} \int_{A_1} \int_{A_2} \frac{\cos \Phi_1 \cos \Phi_2}{\pi R^2} dA_2 dA_1 \quad (2)$$

where R is the distance between both differential elements dA_1 and dA_2 ; A_1 and A_2 are the faces of both surfaces; ϕ_1 and ϕ_2 are the angles between the normal vectors to both differential elements and the line between their centres (Fig. 2).

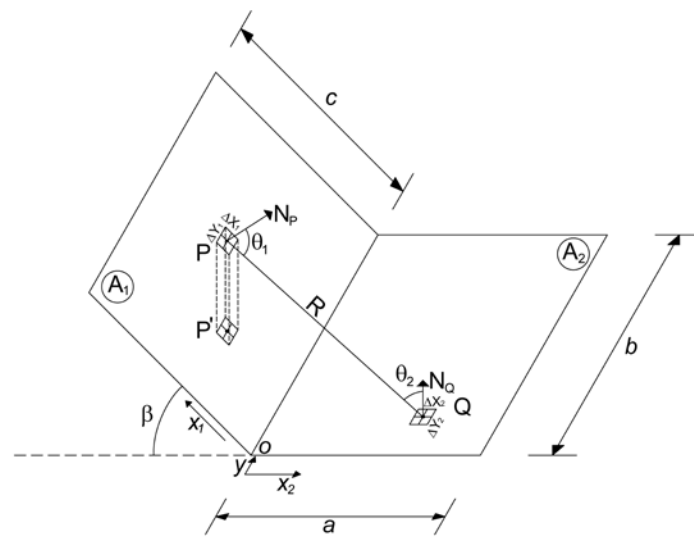


FIG. 1. Isometric view of the receiving (A_1) and emitting (A_2) surfaces

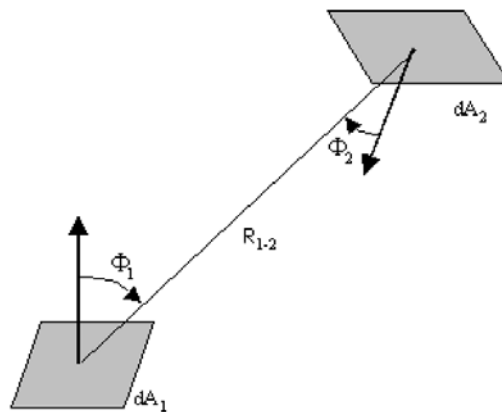


FIG. 2. Defining geometry for configuration factor⁹

In addition, to thermal radiation exchange, view factor also finds its application in the assessment of building cooling load and the design of solar thermal collector and photovoltaic systems where the amount of

incident solar energy from the sun, sky and ground reflections sought. Within that context a differentiation is desirable between configuration and view factors. That differentiation is presented in the following section.

1. Orthogonal case

One of the most revered sources of reference for configuration factor is the text of Siegel and Howell¹⁰. It contains a catalogue of configuration factor for different geometries. The cases, which find ready application with respect to building services, are two rectangular parallel surfaces and surfaces that are perpendicular to each other. The fundamental integral for two rectangular surfaces A_1 with dimensions $a \times b$ and A_2 with dimensions $c \times d$ is Eq. (3):

$$F_{1-2} = \frac{1}{ab} \int_{x_1=0}^a \int_{y_1=0}^b \int_{x_2=0}^c \int_{y_2=0}^d \frac{\cos \Phi_1 \cdot \cos \Phi_2}{\pi R^2} dy_2 dx_2 dy_1 dx_1 \quad (3)$$

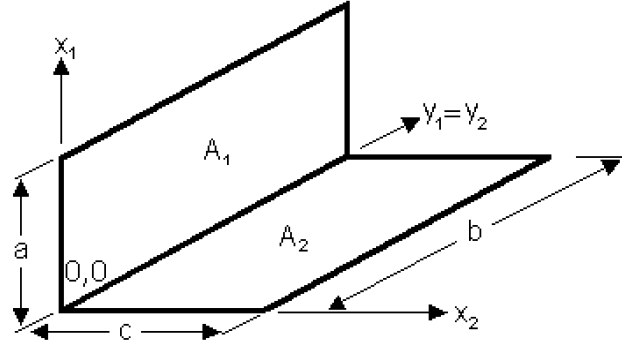


FIG. 3. Two orthogonal surfaces with one common edge

For two perpendicular rectangular surfaces with a common edge b (Fig. 3), where $\cos \Phi_1 = x_2 / R$ and $\cos \Phi_2 = x_1 / R$ and $R = \sqrt{x_1^2 + x_2^2 + (y_1 - y_2)^2}$, the resulting integral is Eq. (4):

$$F_{1-2} = \frac{1}{ab} \int_{x_1=0}^a \int_{y_1=0}^b \int_{x_2=0}^c \int_{y_2=0}^b \frac{x_1 x_2}{\pi [x_1^2 + x_2^2 + (y_1 - y_2)^2]^2} dy_2 dx_2 dy_1 dx_1 \quad (4)$$

The configuration factor – solution of this integral, is Eq. (5), where $N = c / b$ and $L = a / b$:

$$F_{1-2} = \frac{1}{\pi L} \left(L \tan^{-1} \left(\frac{1}{L} \right) + N \tan^{-1} \left(\frac{1}{N} \right) - \sqrt{N^2 + L^2} \tan^{-1} \left(\frac{1}{\sqrt{N^2 + L^2}} \right) + \frac{1}{4} \left\{ \ln \left[\frac{(1 + L^2)(1 + N^2)}{1 + L^2 + N^2} \right] + L^2 \ln \left[\frac{L^2(1 + N^2 + L^2)}{(1 + L^2)(1 + N^2)} \right] + N^2 \ln \left[\frac{N^2(1 + N^2 + L^2)}{(1 + N^2)(N^2 + L^2)} \right] \right\} \right) \quad (5)$$

2. Tilted surface

A more generalised version of the above case is however the one where the two surfaces A_1 and A_2 are not perpendicular to each other. Rather, they are separated by any given angle ϕ that may or may not be 90 degrees, as shown in Fig. 4.

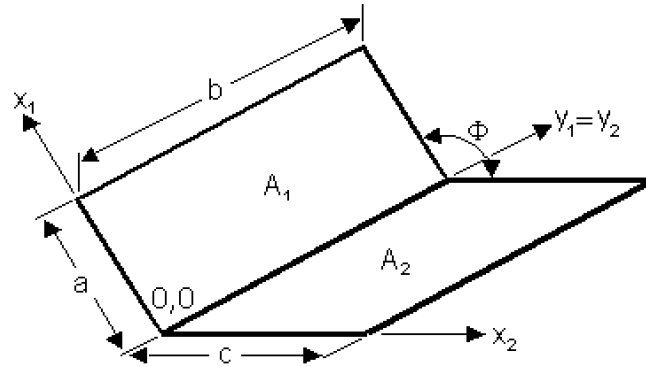


FIG. 4. Two rectangular surfaces with one common edge and included angle of ϕ

This generalised case, once again has a number of applications such as solar energy reflected off ground and incident on a sloping roof, solar thermal water or air collectors or indeed photovoltaic modules. Note that for any given situation the ground reflected radiation may emanate from a conglomeration of surfaces of disparate reflectivities such as grass ($\rho=0.24$), tarmac ($\rho=0.15$), soil ($\rho=0.12-0.25$), other roof tops (0.13), pebbles ($\rho=0.14-0.56$) or water bodies ($\rho=0.05-0.2$).

The integration of Eq. (2) for the case under discussion is rather involved. It does not lead to an exact solution, as was provided for the special case of $\phi = 90^\circ$ – see Eq. (5). It rather leads to a partial, analytically integrable, one part, and the other part that is only numerically obtained.

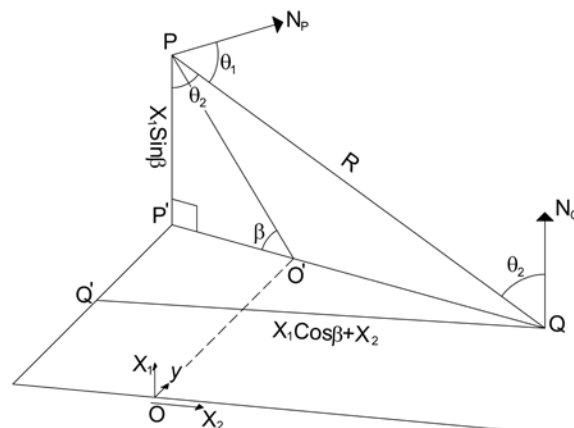


FIG. 5. Projection of A_1 and A_2 surfaces on the X_2/Y and X_2/Z planes

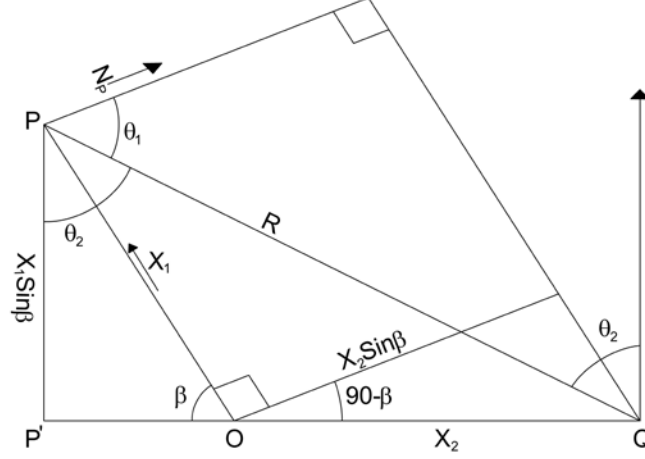


FIG. 6. Detail of projection X_2/Z plane

If we apply Eq. (3) to two rectangular surfaces A_1 with dimensions $a \times b$ and A_2 with dimensions $c \times b$, with angle ϕ between them (Fig. 5 and Fig. 6), then $\beta = \pi - \phi$, $\cos \Phi_1 = x_2 \sin \beta / R$ and $\cos \Phi_2 = x_1 \sin \beta / R$ and $R = \sqrt{x_1^2 + x_2^2 + 2x_1x_2 \cos \beta + (y_1 - y_2)^2}$ and the resulting integral is Eq. (6):

$$F_{1-2} = \frac{1}{ab} \int_{x_1=0}^a \int_{y_1=0}^b \int_{x_2=0}^c \int_{y_2=0}^b \frac{x_1 x_2 \sin^2 \beta}{\pi [x_1^2 + x_2^2 + 2x_1 x_2 \cos \beta + (y_1 - y_2)^2]^2} dy_2 dx_2 dy_1 dx_1 \quad (6)$$

The solution of this integral is Eq. (7), where $A = c/b$, $B = a/b$, $C = A^2 + B^2 - 2AB \cos \Phi$ and

$$D = \sqrt{1 + A^2 \sin^2 \Phi} \quad (7)$$

$$\begin{aligned} F_{1-2} = & -\frac{\sin 2\Phi}{4\pi B} \left[AB \sin \Phi + \left(\frac{\pi}{2} - \Phi \right) (A^2 + B^2) + B^2 \tan^{-1} \left(\frac{A - B \cos \Phi}{B \sin \Phi} \right) + A^2 \tan^{-1} \left(\frac{B - A \cos \Phi}{A \sin \Phi} \right) \right] \\ & + \frac{\sin^2 \Phi}{4\pi B} \left\{ \left(\frac{2}{\sin^2 \Phi} - 1 \right) \ln \left[\frac{(1 + A^2)(1 + B^2)}{1 + C} \right] + B^2 \ln \left[\frac{B^2(1 + C)}{C(1 + B^2)} \right] + A^2 \ln \left[\frac{A^2(1 + A^2)^{\cos 2\Phi}}{C(1 + C)^{\cos 2\Phi}} \right] \right\} \\ & + \frac{1}{\pi} \tan^{-1} \left(\frac{1}{B} \right) + \frac{A}{\pi B} \tan^{-1} \left(\frac{1}{A} \right) - \frac{\sqrt{C}}{\pi B} \tan^{-1} \left(\frac{1}{\sqrt{C}} \right) \\ & + \frac{\sin \Phi \sin 2\Phi}{2\pi B} AD \left[\tan^{-1} \left(\frac{A \cos \Phi}{D} \right) + \tan^{-1} \left(\frac{B - A \cos \Phi}{D} \right) \right] \\ & + \frac{\cos \Phi}{\pi B} \int_0^B \sqrt{1 + z^2 \sin^2 \Phi} \left[\tan^{-1} \left(\frac{z \cos \Phi}{\sqrt{1 + z^2 \sin^2 \Phi}} \right) + \tan^{-1} \left(\frac{A - z \cos \Phi}{\sqrt{1 + z^2 \sin^2 \Phi}} \right) \right] dz \end{aligned} \quad (7)$$

The last part of Eq. (7) is unsolvable integral. This explains why a complete analytical solution of Eq. (6) does not exist. The view factor F_{1-2} can be estimated partially analytically, partially numerically.

The object of this article is to present a mathematical formulation for the differential elements shown in Fig. 1. By numerically integrating the elemental view factor it is then possible to obtain *GVF* for surface A_1 . Note that a fragmented set of reflectivity data for the foreground (surface A_2) can be easily handled in this

approach, an example of which is presented towards the end of this article. Furthermore, a Visual Basic for Application (VBA) code is presented that would enable the reader to obtain the *GVF* for any given geometry and choice of reflectivities for the foreground (surface A_2).

B. Comparison and difference between configuration factor and view factor

Configuration factor (*CF*): The configuration factor F_{i-j} is defined as the fraction of diffusely radiated energy leaving surface A_i that is incident on surface A_j . It is estimated with Eq. (2).

The configuration factor F_{i-j} participates in the product $A_i F_{i-j} I_i$ that reflects the energy flux uniformly emitted from surface A_i to surface A_j . There I_i is the value of the emitted irradiance from surface i . From the view point of surface A_j , the product $A_j F_{j-i} I_i$ is the energy flux received by surface A_j from uniformly emitting surface A_i . Even from different viewpoints, both expressions estimate the same flux of energy and this easily leads to a reciprocity relation between both factors.

By above definition F_{i-j} means that surface A_i is emitting, surface A_j is receiving, thus the configuration factor F_{i-j} is "viewing" from the position of the emitting surface A_i . In other words F_{i-j} represents how well the surface A_i sees surface A_j and explains why F_{i-j} is not equal to F_{j-i} .

In building facade energy exchange we usually need "viewing" from the position of the receiving surface. This is why the definitions and values of the configuration factor and from other side Sky View Factor (*SVF*) and Ground View Factor (*GVF*) are different.

Sky view factor (*SVF*): By definition, *SVF* is the ratio of the sky radiation received by a surface A to the radiation emitted by the entire sky hemispheric environment. In other words *SVF* represents how well the surface sees the sky hemisphere. The approach presumes that the sky hemisphere is uniformly emitting. The concept is applied in the estimation of the background diffuse irradiance on a surface, although the diffuse radiance actually has an anisotropic nature. On the other hand the approach is suitable to be used in the estimation of building heat loss through radiation to the sky hemisphere. The relationship between *SVF* and *CF* is given by Eq. (8):

$$SVF = CF (AREA_{emitting} / AREA_{receiving}) \quad (8)$$

Ground view factor (*GVF*) is the ratio of the reflected ground radiation received by a planar surface to radiation emitted by the entire hemispheric ground environment. The widely used isotropic constant model

(ICM) of Liu and Jordan¹² for estimation of the reflected irradiance assumes a constant albedo and needs a ground view factor (*GVF*), which we can estimate from the value of *CF* as follows:

$$GVF = CF (AREA_{emitting} / AREA_{receiving}) \quad (9)$$

The reflected irradiance I_i depends on the global horizontal irradiance I_{GH} and the albedo ρ – Eq. (10):

$$I_i = \rho I_{GH} \quad (10)$$

The total reflected radiation R_R , received by the surface A_j from the uniform reflecting surface A_i is estimated with Eq. (11):

$$R_R = \rho I_{GH} A_i F_{i-j} = \rho I_{GH} A_j F_{j-i} = \rho I_{GH} A_j GVF \quad (11)$$

If we need to study the 2D-variations in the incident irradiance, it's better to use the third variant of this equation: $R_R = \rho I_{GH} A_j GVF$

C. View factor algebra

The view factor algebra is a combination of basic configuration factors between surfaces with different geometries and some fundamental relations between them⁹:

- **Superposition rules:** Two superposition rules could be defined for the view factors to surfaces. They help to estimate the view factors which cannot be evaluated directly.

Rule 1: The product of the view factor F_{i-j} from a surface i to surface j and the area A_i of surface i is equal to the sum of the products of the view factors from the parts of surface i to surface j and their areas.

$$F_{i-j} A_i = \sum_{k=1}^N F_{i_k-j} A_{i_k} \quad (12)$$

Rule 2: The view factor F_{i-j} from a surface i to surface j is equal to the sum of the view factors from the surface i to the parts of the surface j .

$$F_{i-j} = \sum_{k=1}^N F_{i-j_k} \quad (13)$$

- **Summation rule:** The sum of the view factors from a given surface in an enclosure, including the possible self-view factor for concave surfaces, is 1.
- **Reciprocity relation:** A reciprocity relation between two opposite view factors of two isotropic emitting / receiving surfaces exists and allows the calculation of a view factor from the knowledge of its reciprocal:

$$A_i F_{i-j} = A_j F_{j-i} \quad (14)$$

- **Bounding:** View factors are bounded to $0 \leq F_{i-j} \leq 1$ by definition.

New derivative view factors can be computed from a set of known factors with the help of the mentioned fundamental relations. Let us check this possibility with some exemplary configurations.

Configuration 1: Let us have two rectangular surfaces i and j with a common edge and each of them have two rectangular parts: $A_i = A_{i_1} + A_{i_2}$ and $A_j = A_{j_1} + A_{j_2}$ (Fig. 7). Let us apply View Factor Analysis (VFA) to estimate F_{i-j_1} – the VF from the horizontal rectangle i to the left part j_1 of the inclined surface j :

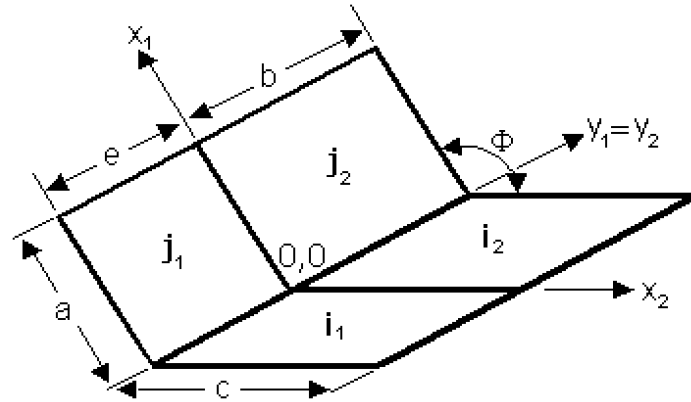


FIG. 7. Configuration 1 – two rectangular surfaces i and j with one common edge. The VF of the parts of the surface i (i_1 and i_2) to the opposite parts (j_2 and j_1) of the surface j are in a relationship – Eq. (17).

$$F_{i_2-j_1} = \frac{1}{bc} \int_{x_2=0}^c \int_{y_2=0}^b \int_{x_1=0}^a \int_{y_1=-e}^0 \frac{\cos \theta_i \cdot \cos \theta_j}{\pi R^2} dy_1 dx_1 dy_2 dx_2 \quad (15)$$

$$F_{i_1-j_2} = \frac{1}{ec} \int_{x_2=0}^c \int_{y_1=-e}^0 \int_{x_1=0}^a \int_{y_2=0}^b \frac{\cos \theta_i \cdot \cos \theta_j}{\pi R^2} dy_2 dx_1 dy_1 dx_2 \quad (16)$$

If we compare last two Eqs. (15) and (16) we could see the relationship between these view factors – Eq. (17):

$$b \cdot F_{i_2-j_1} = e \cdot F_{i_1-j_2} \quad (17)$$

This relationship, added to the other relationships between the view factors, can help us to compute derivative view factors like F_{i-j_1} :

$$F_{i-j_1} = \frac{1}{2} \left(F_{i-j} + \frac{e}{e+b} F_{i-j_1} - \frac{b}{e+b} F_{i_2-j_2} \right) \quad (18)$$

Note: F_{i-j} is F_{i_1, i_2-j_1, j_2}

Configuration 2: Let us have two rectangular surfaces i and j with a common edge and let each of them have three rectangular parts: $A_i = A_{i_1} + A_{i_2} + A_{i_3}$ and $A_j = A_{j_1} + A_{j_2} + A_{j_3}$ (Fig. 8). Let us apply VFA to estimate F_{i-j_2} :

If we apply the Eq. (18) to the surfaces in our configuration 2, where $d=e+b+f$, we can express the derivative view factors F_{i-j_1} , F_{i-j_2} and F_{i-j_3} with the help of the basic view factors:

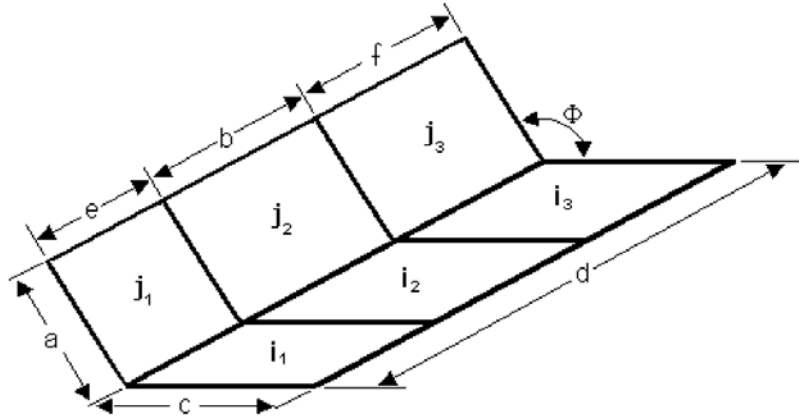


FIG. 8. Configuration 2 – two rectangular surfaces i and j with one common edge. The VF of the part j_2 of the surface j to the whole surface i can be estimated with the help of view factor algebra – Eq. (22).

$$F_{i-j_1} = \frac{1}{2} \left(F_{i-j} + \frac{e}{d} F_{i_1-j_1} - \frac{b+f}{d} F_{i_2+j_2+j_3} \right) \quad (19)$$

$$F_{i-j_3} = \frac{1}{2} \left(F_{i-j} + \frac{f}{d} F_{i_3-j_3} - \frac{e+b}{d} F_{i_1+j_1+j_2} \right) \quad (20)$$

$$F_{i-j_2} = \frac{1}{2d} \left[(e+b) F_{i_1+j_1+j_2} + (b+f) F_{i_2+j_2+j_3} - f F_{i_3-j_3} - e F_{i_1-j_1} \right] \quad (21)$$

If j_2 is the receiving surface, the derivative view factor F_{j_2-i} is more useful:

$$F_{j_2-i} = \frac{1}{2b} \left[(e+b) F_{j_1+j_1+j_2} + (b+f) F_{j_2+j_2+j_3} - f F_{j_3-i_3} - e F_{j_1-i_1} \right] \quad (22)$$

Configuration 3: Let us have two rectangular surfaces with a common edge, separated by given angle ϕ , and let each of them have six rectangular parts: $A_{123456} = A_1 + A_2 + A_3 + A_4 + A_5 + A_6$ and $A_{1'2'3'4'5'6'} = A_1' + A_2' + A_3' + A_4' + A_5' + A_6'$ (Fig. 9). We applied the resulting equations from configurations 1 and 2 and view factor algebra and proved the Eq. (23) for the estimation of derivative view factor $F_{1-3'}$ for inclined receiving surface, but the proof will be omitted here because of its length. This equation is presented in¹³ for two perpendicular surfaces.

$$A_1 F_{1-3'} = \frac{1}{2} \left(\begin{aligned} &K_{(123456)^2} - K_{(1256)^2} - K_{(2345)^2} + K_{(25)^2} - K_{(4,5,6)-(1'2'3'4'5'6')} + K_{(56)-(1'2'5'6')} \\ &+ K_{(45)-(2'3'4'5')} - K_{5-(2'5')} - K_{(123456)-(4'5'6')} + K_{(1256)-(5'6')} + K_{(2345)-(4'5')} \\ &- K_{(25)-5'} + K_{(4,5,6)^2} - K_{(56)^2} - K_{(45)^2} + K_{5^2} \end{aligned} \right) \quad (23)$$

The K terms are defined by $K_{m-n} = A_m F_{m-n}$ and $K_{(m)^2} = A_m F_{m-m'}$.

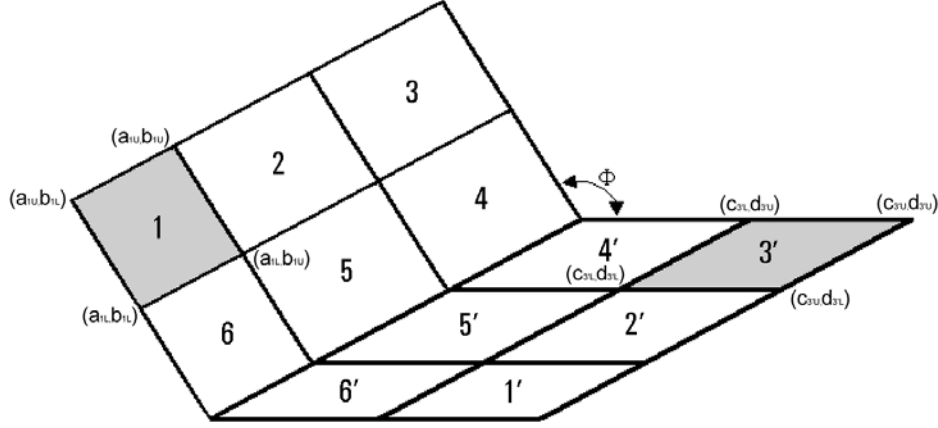


FIG. 9. Configuration 3 – generalized inclined-rectangle arrangement. The VF of part 1 of surface A_{123456} to part 3' of surface $A_{1'2'3'4'5'6'}$ can be estimated with the help of view factor algebra. The coordinates a_{1L} , a_{1U} are along the x_1 axis, the coordinates c_{3L} , c_{3U} are along the x_2 axis, the coordinates b_{1L} , b_{1U} , d_{3L} , d_{3U} are along the $y_1=y_2$ axes

D. Derivation of a numerically integrable, general purpose GVF

If we consider the rectangular surfaces A_i and A_j with a common edge b as composed of many very small rectangular areas (Fig. 10a), we could use numeric integration to receive the same result with a small loss of accuracy:

$$F_{j-i} = \frac{\sin^2 \Phi}{\pi \cdot Na \cdot Nb} \sum_{j_1=1}^{Na} \sum_{j_2=1}^{Nb} \sum_{i_1=1}^{Nc} \sum_{i_2=1}^{Nb} \frac{x_i x_j}{\left[x_i^2 + x_j^2 - 2x_i x_j \cos \Phi + (y_i - y_j)^2 \right]^{3/2}} \Delta c \Delta b \quad (24)$$

where $\Delta a = a / Na$, $\Delta b = b / Nb$, $\Delta c = c / Nc$ and Na , Nb , Nc are the numbers of intervals for the numeric integration in each dimension. The coordinates of each fragment's center are: for surface $i - x_i=(i_1-0.5)\Delta a$; $y_i=(i_2-0.5)\Delta b$; for surface $j - x_j=(j_1-0.5)\Delta a$; $y_j=(j_2-0.5)\Delta b$. Such solution has one main significant advantage – it easily can be adapted for any disposition of both rectangular surfaces (Fig. 10b), but also has two serious disadvantages – it gives an approximate result and to avoid this with large numbers of intervals, it needs a lot of computing time.

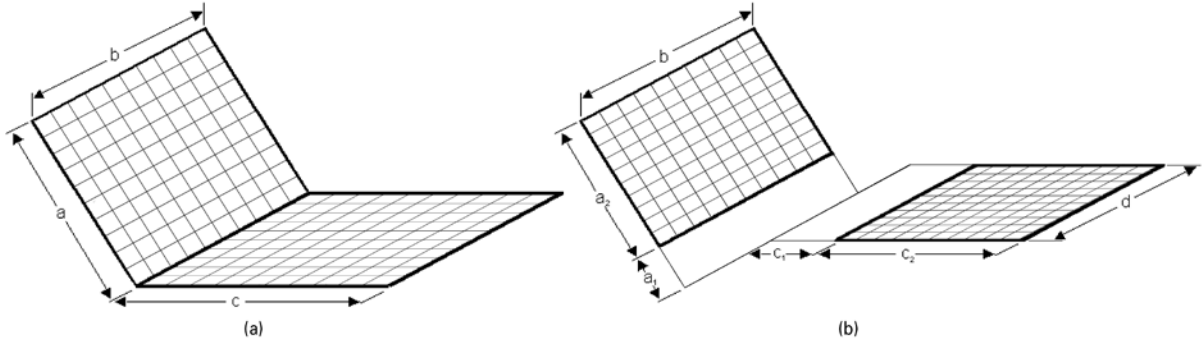


FIG. 10. The reflecting and receiving surfaces are divided in two directions to receive a regular perpendicular grid: (a) both surfaces have one common edge; (b) both surfaces are non-intersecting.

In case of non-uniform reflectivities of the reflecting surface (Fig. 11), such approach is irreplaceable. Let us divide the non-uniform reflecting rectangular surface in an orthogonal grid and to estimate the average albedo value for each cell of this grid. The *GVF* from surface A_j to ground surface A_i , corrected with the albedo values, is given by Eq. (25):

$$F'_{j-i} = \frac{\sin^2 \Phi}{\pi ab} \sum_{j_1=1}^{Na} \sum_{j_2=1}^{Nb} \sum_{i_1=1}^{Nc} \sum_{i_2=1}^{Nd} \frac{x_i x_j \rho_i}{\left[x_i^2 + x_j^2 - 2x_i x_j \cos \Phi + (y_i - y_j)^2 \right]^{3/2}} \Delta a \Delta b \Delta c \Delta d \quad (25)$$

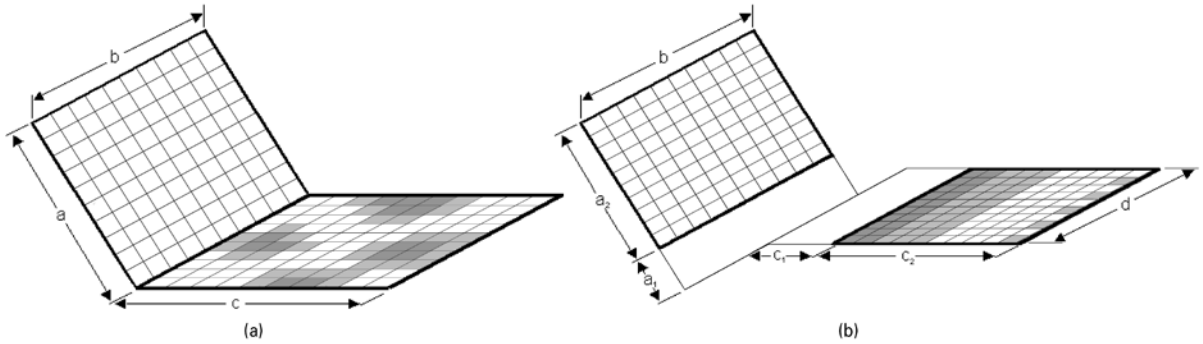


FIG. 11. Case with a non-uniform reflecting surface: (a) both surfaces have one common edge; (b) both surfaces are non-intersecting.

Two interesting studies by Walton^{14, 15} are dedicated to the numerical calculation of radiation view factors between plane convex polygons with obstructions. In the first work¹⁴ he found that Gaussian integration (quadrature) improves the accuracy of the numerical integration. This means that the function is evaluated at specially selected points instead of uniformly distributed points. Such non-uniform spacing can also be used in evaluating area integrals. In next section we will describe our experience and results with improved accuracy when a non-uniform spacing is used for numerical contour integration.

III. COMPUTATIONAL TOOL DEVELOPMENT

In the present work, using Eqs. (24) and (25), four sets of numerically integrating codes were developed to obtain GVF . These four codes represent the evolution of the present work and demonstrate the code architecture from being simple-most and yet of low efficiency to highly-efficient but more complex. Those cases are:

A. Uniform grid

A uniform grid, where all cells within the emitting plane are of same dimension and aspect ratio, is applied on the reflecting surface. Likewise, the cells within the receiving plane have similar properties. The lengths of cells within the emitting and receiving planes may or may not be equal. Square grids for both surfaces show better accuracy in the estimating of VF . This approach can be easily applied as on a combination of two surfaces with one common edge (Fig. 10a), as on a combination of two non-intersecting rectangular surfaces that are inclined to each other (Fig. 10b). For square cells the total number of cells on the receiving surface is $N_{receiving_cells} = (b/a).N_a^2$, and the total number of iterations is $N_{receiving_cells}.N_{emitting_cells}$. This approach does not allow to reach a high accuracy for surfaces, where size a is 10 or more times less than size b and c . On the other hand it is easy to be expanded to deal with a non-uniform reflectivity.

B. Arithmetic Progression

A non-uniform grid in which the cell dimensions increase in an arithmetic progression as one moves from the common edge (Fig. 12). This development was undertaken once the nature of influence of cells receding from the common edge was systematically studied within the present work. The shape of each cell is as close as possible to a square. This is especially important for the cells in the rows that are closer to the common line, because any other proportion of these cells generates significant errors in the result. The size of cell in first row of both surfaces is equal to the step in the arithmetic progression. The algorithm is the same for a composition of two surfaces with common edge (Fig. 12a) and for a composition of non-intersecting rectangular surfaces that are inclined to each other (Fig. 12b). The number of square cells on the receiving surface as on Fig. 12a is $N_{receiving_cells} = (b/a).N_a.(N_a + 1).(1+1/2+1/3+...+1/N_a)/2$, the number of square cells on the receiving surface as on Fig. 12b is $N_{receiving_cells} = (b/a_2).N_a.(N_a + 1).(1+1/2+1/3+...+1/N_a)/2$. The number of square cells on the emitting surface can be estimated by analogy. The total number of iterations is $N_{receiving_cells}.N_{emitting_cells}$. While

this approach gives very accurate results for the first composition, its accuracy for the second composition is not good enough, regardless the high number of iterations. This leads us to another version of this approach.

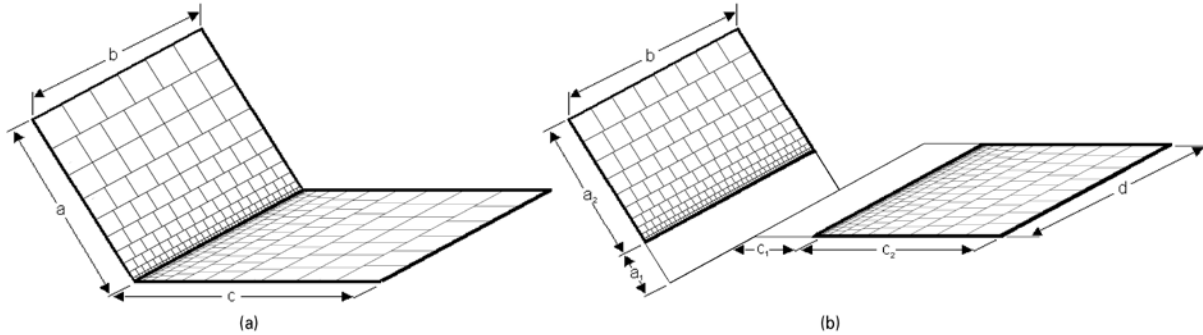


FIG. 12. A non-uniform grid, where cell sizes increase in arithmetic progression, could be applied on: (a) two rectangular surfaces with one common edge; (b) two non-intersecting rectangular surfaces that are inclined to each other

C. Proportional Arithmetic Progression

The analysis of the accuracy for the previous approach for non-intersecting rectangular surfaces shows that cell size and number of cells in a row have to be in relation to the distance from the common line of both planes and to increase slowly. It is suitable the size of cells in first row to be equal to the step in the arithmetic progression only when the surface is adjoining to the common edge (Fig. 13a and 13b), else the cells in the first row need to have bigger size, proportional to its distance from the common line of both planes (Fig. 13c and 13d). The first step is to estimate the number of virtual rows N_{a0} in the interval between the common line of both planes and the lower edge of the receiving surface. The number of square cells on a receiving surface as on Fig. 13a is the same as for the previous approach. The number of square cells on the receiving surface on Fig. 13c is $N_{receiving_cells} = [b/(a_1+a_2)].(N_a+N_{a0}).(N_a+N_{a0}+1).[1/(N_{a0}+1)+1/(N_{a0}+2)+...+1/(N_{a0}+N_a)]/2$. The number of square cells on the emitting surface can be estimated by analogy. The total number of iterations is $N_{receiving_cells}.N_{emitting_cells}$.

It is interesting to see that this approach with lower number of considered cells and iterations gives better results than the previous approach. The conclusion is the bigger numbers of cells (iterations) does not always mean better accuracy. It is important where the grid is more close-meshed and how much in comparison with other parts of the surface. Last two approaches are especially better in comparison with uniform grid approach for surfaces, where size a is 10 or more times less than size b and c .

More details and a pictorial comparison of last two algorithms are given on Figs. 15 and 16 with a flow-diagram for the cell generation. In the following section the above three procedures for cell generation shall be validated using data and examples presented by earlier researchers.

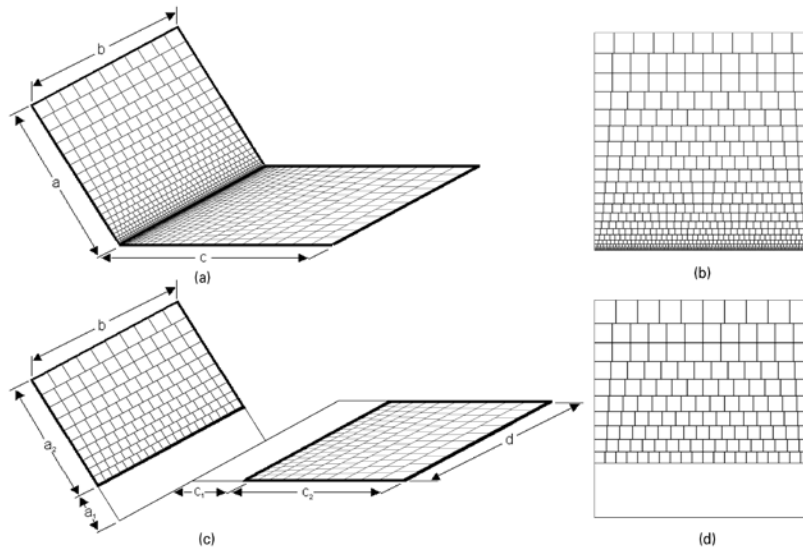


FIG. 13. A non-uniform grid, where cells increase in a proportional arithmetic progression, could be applied on (a) two rectangular surfaces with one common edge; (b) grid for receiving surface with $N_a=20$ rows of cells; (c) two non-intersecting rectangular surfaces that are inclined to each other; (d) grid for receiving surface with $N_a=10$ rows of cells.

D. Combined approach

The proportional-arithmetic-progression approach is suitable to be applied on a receiving surface. On other hand sometimes it is difficult to be applied on the non-uniform emitting surface, where the regular grid is more convenient. A combined approach can unite the advantages of both approaches (high accuracy and easy preparing of the foreground albedo matrix) and to decrease their disadvantages (Fig. 14). The resulting number of iterations and corresponding computer time will be lower than for the previous two approaches, based only on irregular grids.

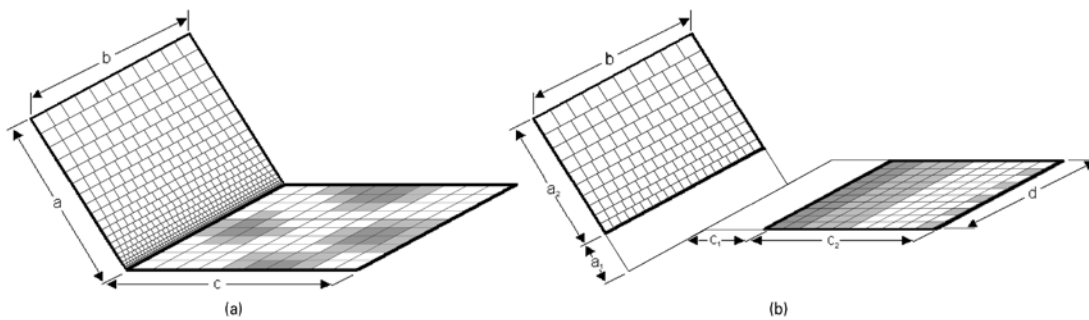


FIG. 14. A combination of non-uniform grid for the receiving surface and a uniform grid for the emitting surface with non-uniform reflectivity: (a) two rectangular surfaces with one common edge; (b) two non-intersecting rectangular surfaces that are inclined to each other.

E. Example 1

Consider the front row of a solar PV farm. The length of the row is 10 m and the modules are inclined at an angle of 45 degrees from the horizontal; the height of the modules is 2 m. The bottom edge of the modules is

1 m from the ground, measured along the plane of the module. To enhance ground-reflected radiation, white pebbles ($\rho = 0.6$) are laid out in-between the rows and in front of the first row from a distance of 1 – 5 m from the common edge, the rest of the horizon being grass ($\rho = 0.24$). Using the analysis presented in this article calculate the ground-reflected radiation that is incident upon the PV modules. Considering only the first 20 m of the horizon for your analysis, obtain the relative reflected-energy contribution from each of the two grass and pebble-bed surfaces (Fig. 15). The horizontal irradiation is given as 800 W/m^2 .

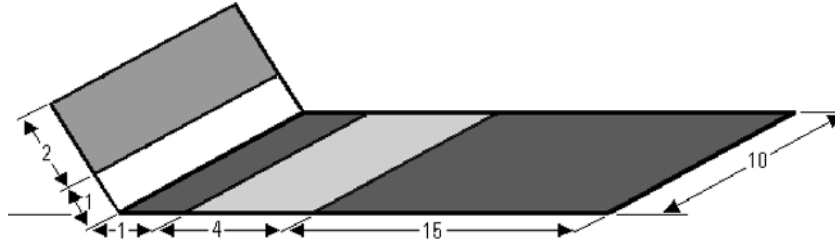


FIG. 15. Schematic image for example 1.

Solution

We shall deal with this analysis, considering the three parts of the foreground: part I being the grass rectangle that extends from 0 – 1 m from common edge, then the pebble bed that lies between 1 – 5 m and finally the rest of the grass from 5 – 20 m.

Part I:

Step 1 Refer to Fig. 9. We can readily identify the following coordinates for the analysis:

For first (near-to-PV modules) grass rectangle $a_{1L}=1$, $a_{1U}=3$, $b_{1L}=0$, $b_{1U}=10$, $c_{1L}=0$, $c_{1U}=1$, $d_{1L}=0$ and $d_{1U}=10$. Then using Eq. (25) and setting up the mesh with $N_a=10$ the algorithm shown in Fig. 17 and 18 may be used to generate the PV module mesh. Likewise, with $N_c=10$ the albedo matrix for the emitting surface (foreground) can be created easily. The above procedure is executed through the macro 'Step1_GVF' which is part of the software provided in Dropbox¹⁶:

<https://www.dropbox.com/sh/8eehqf5szu1u68x/AAD4z7GFYkztzf-VgUqvHg7ea?dl=0>

Step 2 Next, the emitting surface (foreground) mesh is generated by running the macro 'Step2_generatecells'.

Step 3 Finally, the ground-reflected radiation is computed by running the third macro 'Step3_GVF'.

Note that the above three steps are repeated for respectively obtaining ground-reflected radiation from pebble-bed and the farther grass field by repeating the above three steps. The relevant parametric details are provided below:

Part II: For pebble-bed $a_{1L}=1$, $a_{1U}=3$, $b_{1L}=0$, $b_{1U}=10$, $c_{1L}=1$, $c_{1U}=5$, $d_{1L}=0$ and $d_{1U}=10$.

Part III: For the second (farthest) grass rectangle $a_{1L}=1$, $a_{1U}=3$, $b_{1L}=0$, $b_{1U}=10$, $c_{1L}=5$, $c_{1U}=20$, $d_{1L}=0$ and $d_{1U}=10$.

The user ought to obtain the following answers:

Part I: Ground-reflected radiation from the first grass rectangle = 3 W/m² of PV module (GVF=0.004).

Part II: Ground-reflected radiation from pebble-bed = 22 W/m² of PV module (GVF=0.028).

Part III: Ground-reflected radiation from the second grass rectangle = 4 W/m² of PV module (GVF=0.005).

The total reflected radiation is thus 29 W/m² of which 76% is contributed by the pebble bed of 4 m length.

IV. RESULTS, VALIDATION AND DISCUSSION

Hamilton and Morgan¹⁷ were the first team to present, among other cases, view factor analysis for surfaces that share a common edge and are at an angle to each other. The latter work was then further improved in terms of accuracy by Feingold¹⁸ who also presented tables for view factors for surfaces with a common edge and inclined to each other at various angles. The above two works of reference have been catalogued by Siegel and Howell¹⁰ who also provide software for obtaining view factor. The limitation however with the latter is that the solution can only be obtained for inclined planes that meet at a common edge. Furthermore, the solution is obtained through an analytical route, thus limiting its use when an irregular horizon with varying reflectivity is provided. In the present work a numerical solution is obtained using a finite-element grid which is capable of handling an irregular horizon. The reflectivity data may be provided via a two-dimensional table (see the example file provided on this web address¹⁶). Also presented in this work is the analytical solution for view factor between two non-intersecting surfaces that are inclined to each other (see Eq. (23) and Fig. 9).

With the view to validate the present software, developed within the MS-Excel environment using a Visual Basic for Applications (VBA) tool, Tables I-III have been prepared. The estimated values with our numerical approach were compared with values, received with the analytical approach, described in sections II (A) to II (C) and validated with calculated data, published by Holman¹³, Siegel and Howell¹⁰, Hamilton and Morgan¹⁷, Feingold¹⁸ and Suryanarayana¹⁹.

The chosen view factors are to demonstrate the flexibility of the software to handle integrated- or split surfaces with equal ease. Examples of the former (integrated) case that may be cited are the radiant energy exchange between two walls that have a common edge, or a solar collector (thermal or PV module) that receives

ground-reflected energy. An example of the latter (split surface) may be a window within a room that is exchanging energy with walls or ceiling.

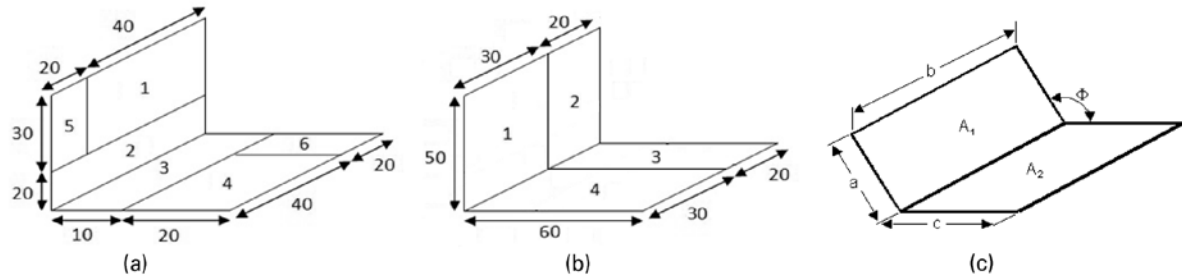


FIG. 16. Schematic images: (a) test case for Table I (surfaces split along ‘a’, ‘b’, ‘c’ and ‘d’), angle 90° and 50 iterations; (b) test case for Table II (surfaces split along ‘b’ and ‘d’), angle 90° and 50 iterations; (c) test case for Table III.

Note that in all cases presented within Tables I and II the difference between the analytical and numerical solution is under **0.055%**. The accuracy figures for Table III exceed **99.9%**. If however, a higher accuracy is required then the number of iterations may be increased. Note also that for surfaces that are at an acute angle to each other (see case 1 within table III) a slightly higher grid resolution is required to achieve appropriate accuracy.

Table I. Evaluation and validation of the numerical model with combined grid: Test case 1 – Fig. 16a – surfaces split along ‘a’, ‘b’, ‘c’ and ‘d’, $N_a=50$, $N_c=50$, $N_d=50$, angle 90° . Sub-cases 1, 3, 5, 7 are based on¹⁷ and compared with the results there.

Number	Sub Case	GVF numeric	GVF analytic	No of iterations	Error %	Time ^a , s
1	F _{2-4,6}	0.12279722	0.12277560	43102500	0.018%	59
2	F _{1-4,6}	0.07002322	0.07001912	8552500	0.006%	12
3	F _{2-3,4,6}	0.29747763	0.29740258	43102500	0.025%	59
4	F _{1,5-3}	0.01586171	0.01586182	12790000	-0.001%	17
5	F _{1,5,2-3,4,6}	0.16921932	0.16917600	17282500	0.026%	24
6	F ₅₋₆	0.00763796	0.00763791	4305000	0.001%	7
7	F ₂₋₃ ^a	0.17470547	0.17462698	43102500	0.045%	59
8	F ₂₋₃ ^b	0.17470547	0.17462698	43102500	0.001%	62

^aTime for execution on a laptop with 5 GB RAM and 2.67 GHz Intel Core I5 processor

^bTime for execution on a desktop with 4 GB RAM and 3 GHz Intel Core Duo processor

Table II. Evaluation and validation of the numerical model with combined grid: Test case 2 – Fig. 16b – surfaces split along ‘b’ and ‘d’, $N_a=50$, $N_c=50$, $N_d=50$, angle 90° . All sub-cases are based on [17] and compared with the results there.

Number	Sub-case	GVF numeric	GVF analytic	No of iterations	Error %	Time, S
1	F _{1,2-3,4}	0.21117310	0.21116258	14412500	0.005%	20
2	F ₁₋₄	0.17025320	0.17027844	8672500	-0.015%	12
3	F ₂₋₃	0.13803786	0.13809616	5810000	-0.042%	8
4	F ₁₋₃	0.04482170	0.04479754	8672500	0.054%	12
5	F ₂₋₄	0.06722647	0.06719631	5810000	0.045%	8

Table III. Evaluation and validation of the numerical model with combined grid for view factor F_{1-2} : Test case 3 – Fig. 16c, $a=b=c=1, N_a=50, N_c=50, N_d=50$

Number	Angle, ϕ°	GVF numeric	GVF analytic	No of iterations	Error %	Time, s
1	30°	0.61937934	0.61902833	14410000	0.057%	20
2	45°	0.48352731	0.48334770	14410000	0.037%	20
3	60°	0.37100758	0.37090532	14410000	0.028%	20
4	90°	0.20006725	0.20004378	14410000	0.012%	19
5	120°	0.08661359	0.08661500	14410000	-0.002%	20
6	135°	0.04830608	0.04830945	14410000	-0.007%	20
7	150°	0.02134296	0.02134533	14410000	-0.011%	20

The structure of the software is of a general nature and it thus enables incorporation of other cases for planer radiant view factor evaluation.

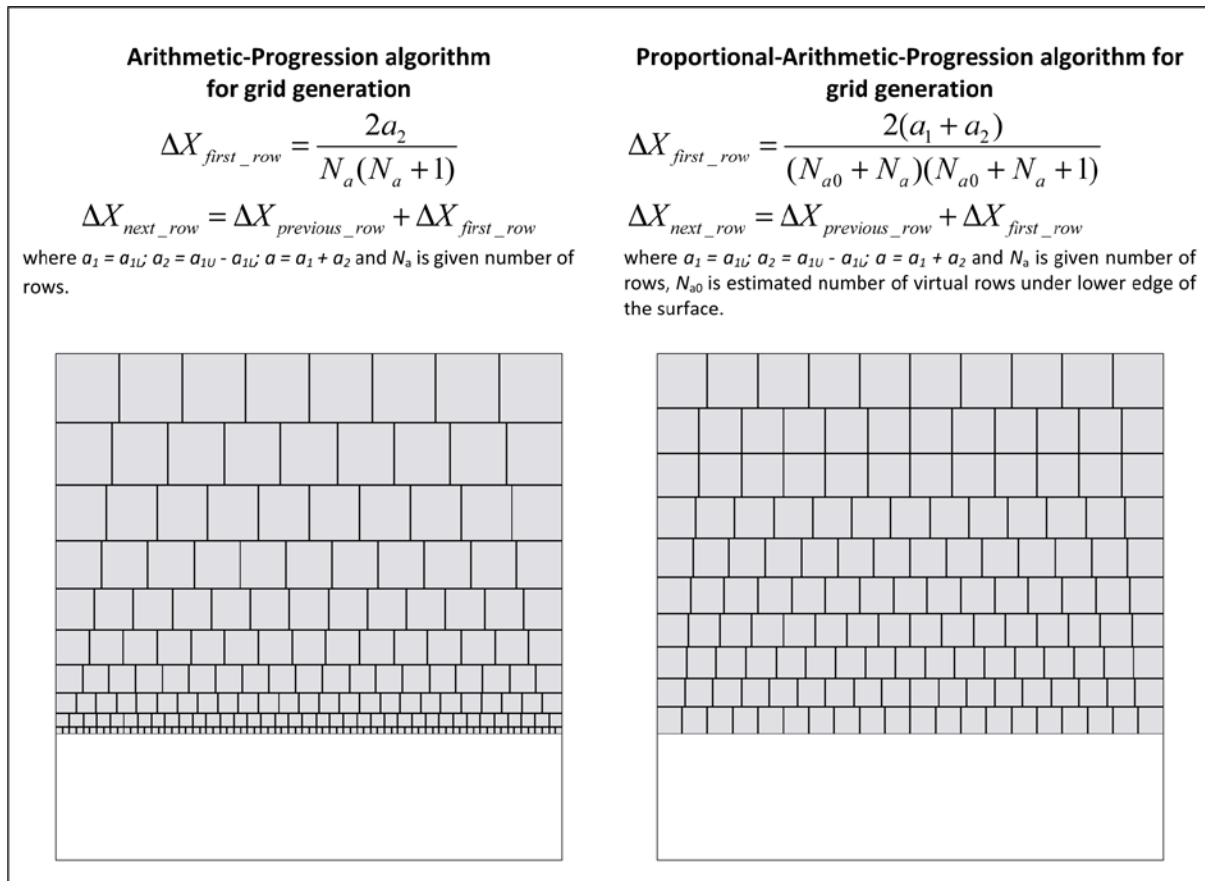
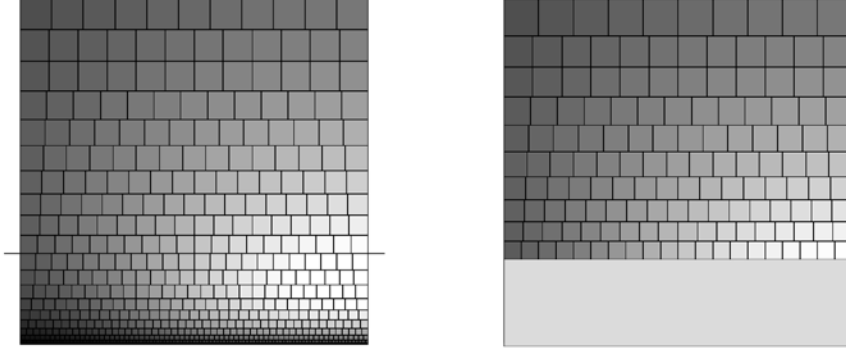


FIG. 17. Pictorial view of the grids, generated by the two algorithms – Arithmetic-Progression and Proportional-Arithmetic-Progression, for two non-intersecting rectangular surfaces. See Fig. 18 for algorithmic details.

Proportional-Arithmetic-Progression algorithm for grid generation

The first step is to find out the number N_{a0} of virtual rows of the area that lie between the common line between the two planes and the given lower edge of the receiving rectangle (under the horizontal line in the left hand image given below):



The RHS is image of the resulting grid of the receiving surface between the lower and upper edges.

In the case shown above, the given number of rows in the receiving surface is $N_a=10$. To estimate N_{a0} we use this double equality:

$$\Delta X_{first_row} = \frac{2(a_1 + a_2)}{(N_{a0} + N_a)(N_{a0} + N_a + 1)} = \frac{2a_1}{N_{a0}(N_{a0} + 1)}$$

where $a_1 = a_{1U}$; $a_2 = a_{1U} - a_{1L}$; $a = a_1 + a_2$. This leads to a quadratic equation for N_{a0} :

$$a_2 N_{a0}^2 + (a_2 - 2a_1 N_a) N_{a0} - a_1 N_a (N_{a0} + 1) = 0$$

We take the larger root which is usually not an integer, so we need to compensate this within the last row of cells. The resulting value of N_{a0} for this example is 10.

$$\Delta X_{first_row} = \frac{2(a_1 + a_2)}{(N_{a0} + N_a)(N_{a0} + N_a + 1)}$$

$$\Delta X_{next_row} = \Delta X_{previous_row} + \Delta X_{first_row}$$

The x-coordinate for all rows, but the first and last rows is given thus,

$$X_{row_i} = X_{row_i-1} + (\Delta X_{row_i-1} + \Delta X_{row_i}) / 2$$

Finally, the compensated last row cells are obtained thus,

$$\Delta X_{last_row} = a_{1U} - (X_{previous_row} + \Delta X_{previous_row} / 2)$$

FIG. 18. Computational flow diagram for generating the grid using Proportional-Arithmetic-Progression procedure.

Refer to Table IV which has been prepared to inter-compare the performance of four currently developed cell-generation algorithms. In the top half of this table the accuracy of three algorithms is presented. To enable a

direct comparison between the algorithms a scoring system has been presently developed. This scoring system, referred as Time-Error-Product, enables algorithmic evaluation, i.e. a low score is sought. The ‘Combined’ algorithm outperforms the ‘Uniform’- and ‘Arithmetic Progression’ algorithms respectively by factors of 22 and 5. Note that for any given geometry when a common edge is shared between the emitting and receiving surfaces the two algorithms, i.e. ‘Arithmetic Progression’ and ‘Proportional Arithmetic Progression’ converge and hence the top half of Table IV only contains the three given algorithms. The lower half of Table IV also presents a comparison of all four algorithms, but for the two surfaces being split, i.e. without a common edge. In this case the performance of ‘Combined and ‘Proportional Arithmetic Progression’ algorithms nearly converge. They are both, however, much more efficient than the ‘Uniform’ and ‘Arithmetic Progression’ models outperforming them by a factor of 5 and 20 respectively (see the final column that provides the TEP figures).

Table IV. Comparison of four mesh generation algorithms with respect to fragments, accuracy for common computer processor time^a

Case	Algorithm	Angle, ϕ°	GVF numeric	GVF analytic	No of iterations	Error %	Time, S	TEP ^b
Table III, Number 2	Arithmetic Progression	45°	0.4838968388	0.4833476997	208022929	0.1136%	296	0.3363
	Uniform	45°	0.5001118731	0.4833476997	33223696	3.4683%	45	1.5607
	Combined	45°	0.4834285373	0.4833476997	83307248	0.0006%	120	0.0696
	Proportional Arithmetic Progression	135°	0.0024743491	0.0024743546	16996540	- 0.0002%	24	0.00005
Table I F ₅₋₆	Arithmetic Progression	135°	0.0024743400	0.0024743547	96978400	- 0.0006%	140	0.00083
	Uniform	135°	0.0024743649	0.0024743547	24010000	0.0004%	33	0.00014
	Combined	135°	0.0024743508	0.0024743547	16459100	- 0.0002%	24	0.00004

^aTime for execution on a laptop with 5 GB RAM and 2.67 GHz Intel Core I5 processor

^bTime-Error-Product (this scoring system enables algorithmic evaluation, i.e. a low score is sought)

The present set of numerical algorithms can easily handle radiation exchange problems where the emitting surface has a non-uniform grid of reflectivities. Very many examples of non-uniform horizon of solar energy collection systems may be cited. In this respect the following web links will illustrate the point under discussion²⁰⁻²⁴. Example 1 presented in Section III (E) is an illustration of the latter subject. Other schematic images of different surface arrangements that fit our approach are presented on Fig. 19. Many of them could be related with different reflecting and receiving surfaces in urban canyons.

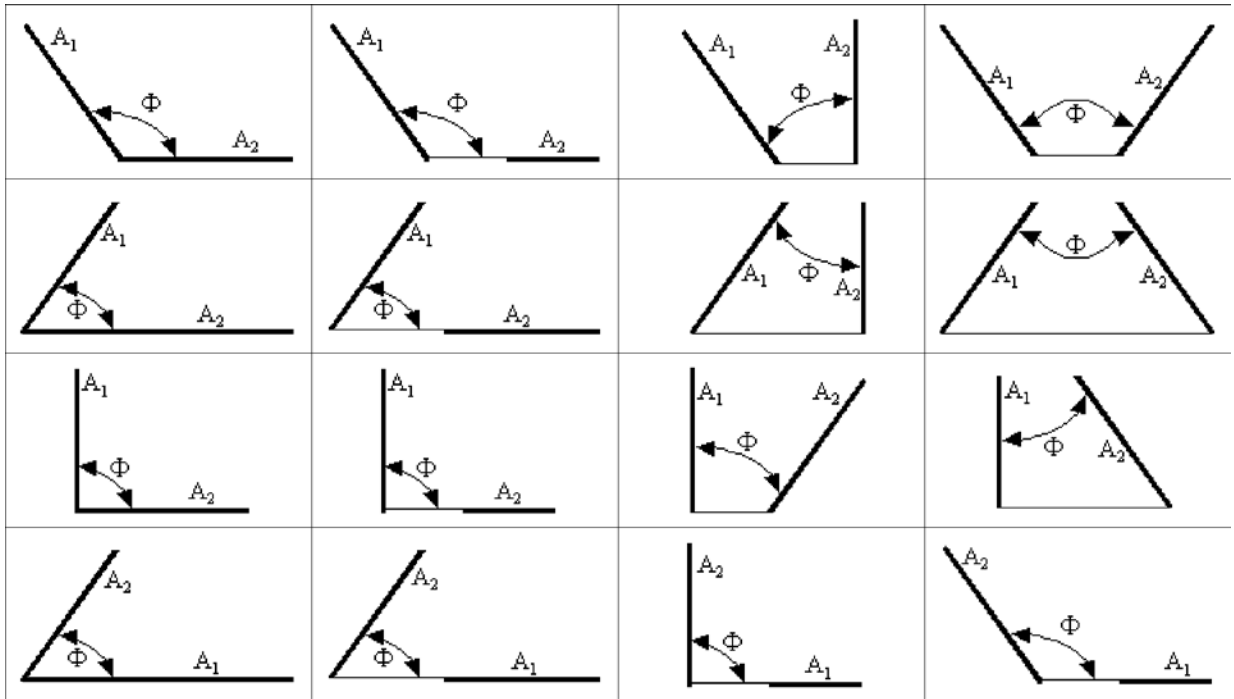


FIG. 19. Schematic images of different surface arrangements that fit our approach. Receiving (A_1) and reflecting (A_2) surfaces are represented with thick solid line, included angle of $\phi < \pi$.

APPENDIX A

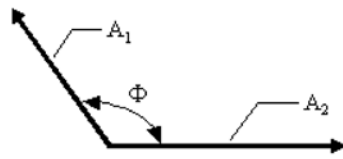
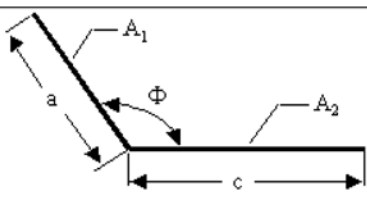
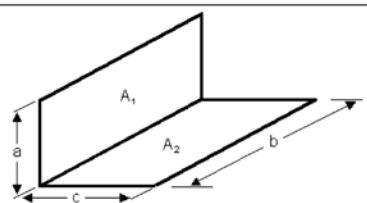
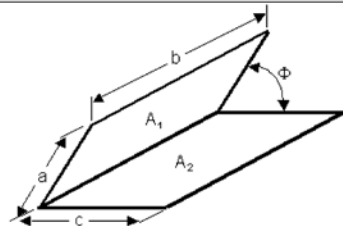
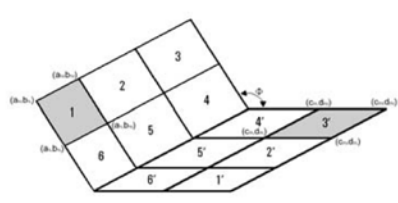
Figure of the defining geometry	Description
	<p>Case (a) Sloping surface of infinite width facing an infinite uniform horizon – the main equation for the analytic estimation of GVF_{1-2} is Eq. (A1). Input data is the included angle ϕ.</p> $GVF = (1 + \cos \phi) / 2 \quad (A1)$
<p>Scheme A1. Defining geometry for case (a)</p>	
	<p>Case (b) Sloping surface of infinite width facing a finite uniform horizon – the main equation for the analytic estimation of GVF_{1-2} is Eq. (A2), where $L = c/a$. Input data are: a, c and included angle ϕ.</p> $GVF = \frac{1 + L - \sqrt{L^2 - 2L \cos \phi + 1}}{2} \quad (A2)$
<p>Scheme A2. Defining geometry for case (b)</p>	
	<p>Case (c90) Vertical surface of finite width facing a finite uniform horizon – the main equation for the analytic estimation of GVF_{1-2} is given as Eq. (5) in section 2.1.1.</p> <p>Input data are: a, b, c.</p>
<p>Scheme A3. Defining geometry for case (c90)</p>	
	<p>Case (c) Sloping surface of finite width facing a finite uniform horizon. The main equation for the analytic estimation of GVF_{1-2} is given as Eq. (7) in section 2.1.2.</p> <p>Input data are: a, b, c and included angle ϕ.</p>
<p>Scheme A4. Defining geometry for case (c)</p>	
	<p>Case (d) View factor for generalized inclined-rectangle arrangement. The analytic estimation of $GVF_{1-3'}$ is based on Eqs. (7) and (23).</p> <p>Input data are: a_{1L}, a_{1U}, $c_{3'L}$, $c_{3'U}$, b_{1L}, b_{1U}, $d_{3'L}$, $d_{3'U}$ and included angle ϕ.</p>
<p>Scheme A5. Defining geometry for case (d)</p>	

FIG. A1. The description of VBA code for analytic estimation of VF includes brief information for each of the given case, its main equation and a figure of the defining geometry (schemes A1-A5).

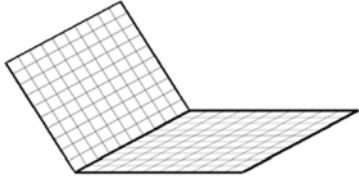
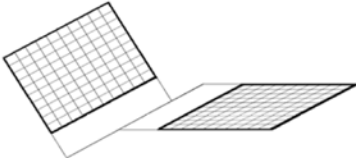
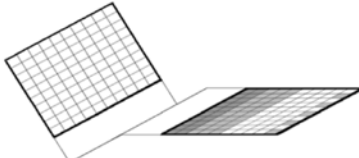
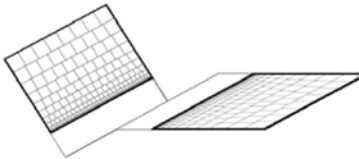
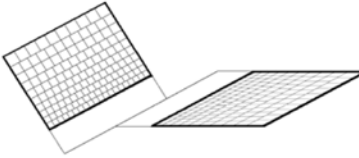
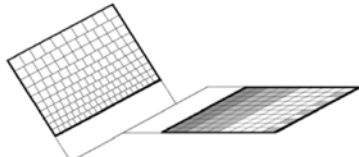
Figure of the defining geometry	Description
	<p>Case (e) Sloping surface of finite width facing a finite uniform horizon, with a common line. The main equation for the numeric estimation of GVF_{1-2} with uniform grid is Eq. (24) in section 2.4.</p> <p>Input data are: a, b, c, included angle ϕ and cell's sizes $delx1, dely1, delx2, dely2$.</p>
<p>Scheme A6. Defining geometry for case (e)</p>	
	<p>Case (f) Sloping surface of finite width facing a finite uniform horizon. The main equation for the numeric estimation of GVF_{1-2} with uniform grid is again Eq. (24) in section 2.4, but applied on different origins of coordinate systems (x_1, y_1) and (x_2, y_2).</p> <p>Input data are: $a_{1L}, a_{1U}, c_{3L}, c_{3U}, b_{1L}, b_{1U}, d_{3L}, d_{3U}$, included angle ϕ and cell's sizes $delx1, dely1, delx2, dely2$.</p>
<p>Scheme A7. Defining geometry for case (f)</p>	
	<p>Case (g) Sloping surface of finite width facing a finite non-uniform horizon. The main equation for the numeric estimation of GVF_{1-2} with uniform grid is Eq. (25) in section 2.4.</p> <p>Input data are: $a_{1L}, a_{1U}, c_{3L}, c_{3U}, b_{1L}, b_{1U}, d_{3L}, d_{3U}$, included angle ϕ and cell's sizes $delx1, dely1, delx2, dely2$. The albedo grid is described with number of intervals along axes x_2 and y_2. The cells with different reflectivities are presented in the worksheet "Albedo matrix".</p>
<p>Scheme A8. Defining geometry for case (g)</p>	
	<p>Case (h) Sloping surface of finite width facing a finite uniform horizon. The non-uniform grid is created with cell's sizes in arithmetic progression (see section 3.2)</p> <p>Input data are: $a_{1L}, a_{1U}, c_{3L}, c_{3U}, b_{1L}, b_{1U}, d_{3L}, d_{3U}$, included angle ϕ and number of cells N_a and N_c.</p>
<p>Scheme A9. Defining geometry for case (h)</p>	
	<p>Case (i) Sloping surface of finite width facing a finite uniform horizon. The non-uniform grid is created with cell's sizes in proportional arithmetic progression (see section 3.3)</p> <p>Input data are: $a_{1L}, a_{1U}, c_{3L}, c_{3U}, b_{1L}, b_{1U}, d_{3L}, d_{3U}$, included angle ϕ and number of cells N_a and N_c.</p>
<p>Scheme A10. Defining geometry for case (i)</p>	
	<p>Case (j) Sloping surface of finite width facing a finite non-uniform horizon. The non-uniform grid of the receiving surface is created with cell's sizes in proportional arithmetic progression (see section 3.4)</p> <p>Input data are: $a_{1L}, a_{1U}, c_{3L}, c_{3U}, b_{1L}, b_{1U}, d_{3L}, d_{3U}$, included angle ϕ and number of cells N_a, N_c and N_d. The reflectivity of emitting surface is described with uniform grid. The information for the cells with different reflectivities is presented in the worksheet "Reflectivity".</p>
<p>Scheme A11. Defining geometry for case (j)</p>	

FIG. A2. The description of VBA code for analytic estimation of VF includes brief information for each of the given case, its main equation and a figure of the defining geometry (schemes A6-A11).

REFERENCES

- ¹Adam Hirsch, Shanti Pless, Rob Guglielmetti and Paul A. Torcellini, The Role of Modeling When Designing for Absolute Energy Use Intensity Requirements in a Design-Build Framework. Available on: http://www.nrel.gov/sustainable_nrel/pdfs/49067.pdf
- ²Hui, S.C.M., Energy Performance of Air-conditioned Buildings in Hong Kong, Thesis, Chapter 6 - Building Energy Simulation Methods, 1996. Available on: <http://web.hku.hk/~cmhui/thesis/chp6.pdf>
- ³G Laccarino, M Fischer and E Hult, Towards Improved Energy Simulation Tools for Buildings: Improving airflow parameterizations within energy simulation using CFD and building measurements, June 22, 2010. Available on: <http://www.iesve.com/content/mediaassets/pdf/p135final-long.pdf>
- ⁴Gianluca Iaccarino, Martin Fischer, Erin Hult, Towards Improved Energy Simulation Tools for Buildings. Improving airflow parameterizations within energy simulation using CFD and building measurements. Available on: <http://www.stanford.edu/group/peec/cgi-bin/docs/buildings/research/Improved%20Energy%20Simulation%20Tools%20for%20Buildings.pdf>
- ⁵Erik DeBenedictis on supercomputing. Available on: <http://intelligence.org/2014/04/03/erik-debenedictis/>
- ⁶High Performance Computing FAQ. Available on: http://www.planethpc.eu/index.php?option=com_content&view=article&id=48
- ⁷The Future of Computing Performance: Game Over or Next Level? Samuel H. Fuller and Lynette I. Millett, Editors; Committee on Sustaining Growth in Computing Performance; National Research Council, Washington DC, 2011
- ⁸BBC NEWS London: 'Walkie-Talkie' skyscraper melts Jaguar car parts. Available on: <http://www.bbc.com/news/uk-england-london-23930675>
- ⁹Howell, J. R., A catalog of radiation heat transfer - configuration factors. Introduction. Available on: <http://www.thermalradiation.net/intro.html>
- ¹⁰Siegel R. and Howell J., *Thermal Radiation and Heat Transfer*, 4th ed. New York: Taylor & Francis, 2002

¹¹Howell, J. R., A catalog of radiation heat transfer - configuration factors. C-16: Two rectangles with one common edge and included angle of Φ . Available on: <http://www.thermalradiation.net/section/C-16.html>

¹²Liu BYH, Jordan RC. The long term average performance of flat plate solar energy collectors. *Solar Energy* 1963;**7**:53–74.

¹³Holman J. P., *Heat Transfer*, 7th edition, McGraw-Hill, New York, 1992

¹⁴Walton, G.N., Algorithms for Calculating Radiation View Factors Between Plane Convex Polygons With Obstructions, National Bureau of Standards, NBSIR 86-3463 (1987 - shortened report in *Fundamentals and Applications of Radiation Heat Transfer*, HTD-Vol.72, American Society of Mechanical Engineers, 1986

¹⁵Walton, G. N., Calculation of obstructed view factors by adaptive integration, Technical Report NISTIR–6925, National Institute of Standards and Technology (NIST), Gaithersburg, MD, 2002

¹⁶Available on: <https://www.dropbox.com/sh/8eehqf5szu1u68x/AAD4z7GFYkztzf-VgUqvHg7ea?dl=0>

¹⁷Hamilton, D. C. and Morgan, W. R. 'Radiant interchange configuration factors', Technical Note 2836, National Advisory Committee for Aeronautics, Washington D.C. (1952)

¹⁸Feingold, A. 'Radiant interchange configuration factors between various selected plane surfaces', *Proc. Royal Society of London, Series A – Mathematical and Physical*, Vol. 292, No. 1428, pp. 51-60 (1966)

¹⁹Suryanarayana N.V., *Engineering Heat Transfer*, West Publishing Company, New York, 1995

²⁰Solar's economics ensure it will be an essential part of the world's future energy mix, Citigroup, August, 2014, Available on: http://www.photon.info/photon_news_detail_en.photon?id=87696

²¹Roberts D., *Energy Democracy: Three Ways to Bring Solar Power to the Masses*, 2012, Available on: <http://www.motherearthnews.com/renewable-energy/community-solar-energy-zwfz1209zhun.aspx#axzz3AIMMkbgS>

²²Chiras D., More Affordable Solar Power, 2012, Available on:

<http://www.motherearthnews.com/renewable-energy/solar-power-zm0z12aszphe.aspx#axzz3AIMMkbgS>

²³Asiis Light, PV soundless – world record “along the highway” – A PV sound barrier with 500 KWp and ceramic based PV modules, 2009, Available on: <http://www.asilin.org/2009/11/pv-soundless-world-record-along-highway.html>

²⁴Alternative Uses of Highway Right-of-Way, Available on:

http://www.fhwa.dot.gov/real_estate/publications/alternative_uses_of_highway_right-of-way/rep03.cfm